Unveiling the intricacies of nonlinear third-harmonic generation within a hyperstructure

Fu-Pei Wu and Hai-Feng Zhang*

College of Electronic and Optical Engineering & College of Flexible Electronics (Future Technology), Nanjing University of Posts and Telecommunications, Jiangsu province, 210023, China

(Received 16 April 2024; accepted 15 July 2024; published 5 August 2024)

In this paper, the propagation characteristics of fundamental and third harmonic waves within the designed hyperstructure are examined using the transfer matrix method. At the same time, the efficiency of third harmonic generation is quantified. The transfer matrix method provides a framework that takes into account the interference phenomena and multiple reflections occurring within each layer, thereby facilitating a precise emulation of the generation and propagation dynamics of the harmonic wave field within the hyperstructure. Moreover, the conspicuous phenomenon of strong field localization, coupled with the lower group delay observed at the edges of the photonic band gap, confers an augmented response time on the process of third harmonic conversion. Consequently, electromagnetic waves situated in close proximity to the band-gap edge experience a heightened conversion efficiency. Comparatively, when juxtaposed against those designed in the other works hinged on conventional quasiphase matching techniques and endowed with similar lengths, the distinctive advantages offered by layered periodic structures manifest in their propensity to establish more precise phase matching conditions and yield higher conversion efficiencies. The crucial role played by third harmonic generation in advancing optical imaging, spectroscopy, biomedical applications, and laser technology is due to its distinct optical characteristics and energy conversion capabilities.

DOI: 10.1103/PhysRevA.110.023505

I. INTRODUCTION

Similar to the existence of an electronic band gap in semiconducting materials, the layered periodic arrangement of dielectric substances, characterized by varying refractive indices, manifests analogous structures of photonic band gaps (PBGs) through the influence of Bragg scattering [1–4]. The applications of diverse materials has greatly expanded research possibilities in hyperstructures (HS) [4], including plasma [5], nonlinear optics [6–8], and other related fields [9]. The most accurate methods currently employed for studying HS include the transfer matrix method (TMM) [10,11], plane wave expansion [12], and so on. Among these, TMM offers a convenient analysis of the internal fields within HS by utilizing matrices with varying parameters to represent the electromagnetic (EM) wave transmission characteristics of different layers. This feature makes TMM computationally efficient and enables its broad application in studying one- [13,14], two-, and three-dimensional [15,16] structures.

With the advancement of investigation into harmonic generation in HS comprised of nonlinear materials [17,18], the theoretical framework surrounding harmonic generation within quasiphase matching (QPM) has been expounded under the constraints imposed by the undepleted pump approximation. Many studies focused on investigating the generation, propagation, and efficiency of second harmonics in HS [19]. The attainment of QPM has been successfully demonstrated in HS [20]. It is widely acknowledged that layered structures manifest Bragg high reflectivity zones within their linear transmission spectrum, which have been experimentally verified to significantly amplify the conversion efficiency of harmonics, as evidenced by most investigations [21,22]. Finite one-dimensional HS offer sharply defined resonances resulting from modal interactions [22] near the Bragg band edge, thereby facilitating the utilization of these resonances to lower the threshold of nonlinear processes and magnify their conversion efficiency [23]. This phenomenon arises due to the high-quality factors associated with these resonant modes, subsequently resulting in intensified localized fields at the edge of the reflection band [23]. Furthermore, resonances induced by Fabry-Perot cavities also serve to augment nonlinear effects, resembling the characteristics of optical bistability [24,25]. The outcomes presented in this study establish a direct correlation between sharper resonance peaks and more substantial enhancements of the local field, thereby yielding heightened nonlinear effects [25]. The TMM, along with its variations, characterizes the physical mechanisms of second harmonic wave (SHW) generation within nonlinear structures. Moreover, it enables the quantification of the SHW field in radiation and the enhancement of the SHW through the alteration of the local mode of the electric field [26,27]. These aforementioned studies have enlightened not only the present paper, but also subsequent research endeavors in this domain. In recent years there has been a growing body of research dedicated to the generation and enhancement of higher-order harmonics in metamaterials, yielding achievements both in theory and experimentation [28–30]. High-order harmonic generation possesses significant application in the field of imaging, and in the study

*Contact author: hanlor@163.com; hanlor@njupt.edu.cn

conducted by Smirnova and colleagues, THW imaging is employed to visualize topological edge states [31]. Nonlinear techniques offer superior contrast, sensitivity, and larger imaging areas when compared to linear imaging methods, thereby ensuring accurate characterization and optimization of topological waveguides [31]. Recently, the high-order harmonic generation has been experimentally observed within condensed matter systems, and the research scope of high-order harmonics has expanded to include conventional semiconductors, topological materials [32–35], and band insulators [36–38].

In this paper, an approach based on the TMM has been proposed to investigate the mechanisms involved in the generation and propagation of THW within the HS. The strong localization of the EM field and reduced group delay (which can alter the phase velocity of the incident pump light and compensate for dispersion effects to some extent, optimizing the phase matching and temporal evolution in nonlinear processes, thereby enhancing energy conversion efficiency [27].) near the PBGs edge of the HS effectively reduce the threshold for THW generation and enhance its efficiency. Importantly, when compared to other works that rely on QPM methodologies and have similar sample dimensions, the HS have significant advantages in achieving improved phase-matching conditions and higher conversion efficiencies.

II. TMM FOR LAYERED-PERIODIC STRUCTURE

The HS under investigation in the presented study comprises a periodic unit consisting of alternating layers of CS_2 [39], a uniform nonlinear material, and K9 glass, which are stacked along the $+z$ direction. The refractive indices of CS_2 and K9 glass are denoted as $n_1^{(m)}$ and $n_2^{(m)}$, respectively, with their corresponding thicknesses represented by d_1 and d_2 (the index $m = 1$ corresponds to the fundamental field, while $m = 3$ represents the THW field). The third-order nonlinear susceptibility of CS_2 is represented by $\chi^{(3)}$. A spatially uniform variation of both linear and nonlinear parameters within the material is assumed. The incident EM wave propagates along the $+z$ direction, with the electric field oriented along the $+x$ direction, and the magnetic field along the $+y$ direction. Representing the forward ($+z$) and backward-propagating ($-z$) waves, $\boldsymbol{E}^+$ and $\boldsymbol{E}^-$, respectively denote the electric fields. For ease of analysis, a total of $N = 50$ periods are considered in the calculations. Due to the refractive index mismatch between the layers, the EM wave encounters reflections at the layer interfaces, giving rise to interference phenomena. As the fundamental wave (FW) propagates through the structure, it induces nonlinear polarization $P^{(NL)}$ within the CS_2 material, acting as a secondary source for the THG [26]. These harmonics are continuously emitted at an angular frequency of $3\omega_1$ until they ultimately emerge from both ends of the HS. By exploiting this process, a TMM is established to systematically investigate the transmission characteristics of TH waves within the HS. Initially, the scenario within a single period unit (n_1n_2) is analyzed before extending the analysis to explore the intricate generation mechanisms of TH waves upon stacking multiple units of the HS.

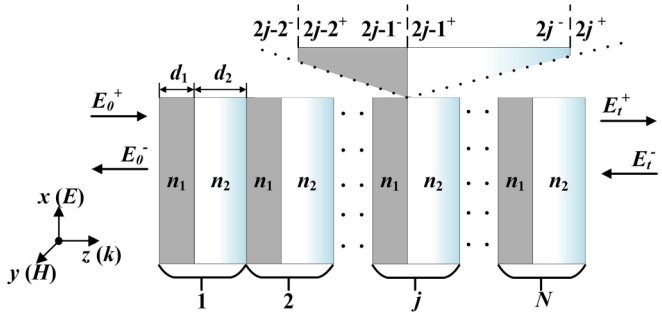

FIG. 1. Schematic diagram of a HS composed of alternating layers of CS_2 and crown glass K9. The periodic unit is denoted by (n_1n_2), with N representing the total number of periods.

A. ANALYSIS OF PERIODIC UNIT

Now, the discourse on the transmission of the FW field in the HS, assuming that FW is incident from the left side of the HS with an angular frequency ω_1. The electric field of the FW within the pth slice can be written as $E_p^{(1)} = E_p^{(1)}(z)\exp(-i\omega_1 t)$ and adheres to the following wave equation Eq. (1), where $k_p^{(1)} = n_p^{(1)}k_0^{(1)}$, $k_0^{(1)} = \omega_1/\mathrm{c}$, $n_p^{(1)}$ represents the refractive index corresponding to the FW field within the pth layer, whereas c denotes the speed of EM wave in vacuum [11]

$$\frac{\mathrm{d}^2E_p^{(1)}}{\mathrm{d}z^2} + k_p^{(1)2}E_p^{(1)} = 0. \tag{1}$$

The $E_p^{(1)}$ can be derived from Eq. (1), and its solution entails both forward- and backward-propagating waves

$$E_p^{(1)}(z) = \Omega_p^{(1)+}e^{ik_p^{(1)}(z-z_{p-1})} + \Omega_p^{(1)-}e^{-ik_p^{(1)}(z-z_{p-1})}, \tag{2}$$

where $z_p = z_{p-1} + d_p$, ($p = 1, 2, 3, \ldots$ and z_0 is set to zero). $\Omega_p^{(1)\pm}$ is the coefficient of $E_p^{(1)}$ at the left interface (z_{p-1}) of the pth layer. From the equation $\nabla \times \boldsymbol{E} = ik_0\,\mathbf{H}$, the magnetic field $H_p^{(1)}(z)$ can be obtained

$$\begin{pmatrix} E_p^{(1)}(z) \\ H_p^{(1)}(z) \end{pmatrix} = \begin{pmatrix} 1 & 1 \\ n_p^{(1)} & -n_p^{(1)} \end{pmatrix} \begin{pmatrix} \Omega_p^{(1)+}(z) \\ \Omega_p^{(1)-}(z) \end{pmatrix}. \tag{3}$$

The continuity of the tangential components of the $\boldsymbol{E}$ and $\boldsymbol{H}$ at the interface of the medium can be expressed by the boundary conditions as follows: $\vec{z} \times (\boldsymbol{E}_{2j-2^-} - \boldsymbol{E}_{2j-2^+}) = 0, \vec{z} \times (\boldsymbol{H}_{2j-2^-} - \boldsymbol{H}_{2j-2^+}) = 0$. A linkage between the fields on both sides of the jth layer in Fig. 1 can be established can be established in Eq. (4), which can be represented using a matrix.

In Eq. (4), the $E^{(1)\pm}$ represents the forward- and backward-propagating waves at different positions within the structure when the periodic unit is placed in air. The composite matrices are defined as

$$\boldsymbol{M}_p = \begin{pmatrix} e^{ik_p^{(1)}d_p} & 0 \\ 0 & e^{-ik_p^{(1)}d_p} \end{pmatrix} \boldsymbol{Q}_p = \begin{pmatrix} 1 & 1 \\ n_p^{(1)} & -n_p^{(1)} \end{pmatrix}.$$

The first matrix characterizes the phase and amplitude fluctuations undergone by the electric field during its propagation across a homogeneous medium, from the left boundary to

the right boundary along the direction of wave transmission. Meanwhile, the second matrix elucidates the interplay between the fields situated on either side of the material interface, which manifests as a direct consequence of the boundary conditions imposed

$$\begin{aligned}
\boldsymbol{Q}_1\begin{pmatrix}E^{(1)+}_{2j-2^+}\\ E^{(1)-}_{2j-2^+}\end{pmatrix} &= \boldsymbol{Q}_0\begin{pmatrix}E^{(1)+}_{2j-2^-}\\ E^{(1)-}_{2j-2^-}\end{pmatrix},\\
\boldsymbol{Q}_2\begin{pmatrix}E^{(1)+}_{2j-1^+}\\ E^{(1)-}_{2j-1^+}\end{pmatrix} &= \boldsymbol{Q}_0\boldsymbol{M}_1\boldsymbol{Q}_1^{-1}\boldsymbol{Q}_0\begin{pmatrix}E^{(1)+}_{2j-2^-}\\ E^{(1)-}_{2j-2^-}\end{pmatrix},\\
\boldsymbol{Q}_0\begin{pmatrix}E^{(1)+}_{2j^+}\\ E^{(1)-}_{2j^+}\end{pmatrix} &= \boldsymbol{Q}_2\boldsymbol{M}_2\boldsymbol{Q}_2^{-1}\boldsymbol{Q}_1\boldsymbol{M}_1\boldsymbol{Q}_1^{-1}\boldsymbol{Q}_0\begin{pmatrix}E^{(1)+}_{2j-2^-}\\ E^{(1)-}_{2j-2^-}\end{pmatrix}.
\end{aligned} \tag{4}$$

Hence, a matrix $\boldsymbol{T}_j$ can be established that links the FW electric fields on both sides of the periodic unit $(n_1 n_2)$,

$$\begin{aligned}
\begin{pmatrix}E^{(1)+}_{2j^+}\\ E^{(1)-}_{2j^+}\end{pmatrix} &= \boldsymbol{Q}_0^{-1}\boldsymbol{Q}_2\boldsymbol{M}_2\boldsymbol{Q}_2^{-1}\boldsymbol{Q}_1\boldsymbol{M}_1\boldsymbol{Q}_1^{-1}\boldsymbol{Q}_0\begin{pmatrix}E^{(1)+}_{2j-2^-}\\ E^{(1)-}_{2j-2^-}\end{pmatrix}\\
&= \boldsymbol{T}_j\begin{pmatrix}E^{(1)+}_{2j-2^-}\\ E^{(1)-}_{2j-2^-}\end{pmatrix}.
\end{aligned} \tag{5}$$

The spatial distribution of the FW across different positions within the periodic unit can be computationally determined by employing Eq. (5). However, the primary objective of this study revolves around investigating the mechanism underlying THW generation. The nonlinear polarization within the nonlinear medium in the pth layer, prompted by the interaction with the FW field, can be mathematically represented as follows [40]:

$$P_p^{NL}(z,t) = \varepsilon_0\chi^{(3)}\left[E_p^{(1)}(z)\right]^3 e^{-i3\omega_1 t}. \tag{6}$$

Unlike the homogeneous Eq. (1) corresponding to the FW, Eq. (7) has a source term on the right-hand side resulting from nonlinear polarization. The wave equation for the THW field is

$$\begin{aligned}
\frac{\mathrm{d}^2E_p^{(3)}(z)}{\mathrm{d}z^2} + k_p^{(3)^2}E_p^{(3)}(z) &= \mu\frac{\partial^2 P_p^{NL}(z,t)}{\partial t^2}\\
&= -\mu\varepsilon_0\chi^{(3)}9\omega_1^2\left[E_p^{(1)}(z)\right]^3\\
&= -\mu\varepsilon_0\chi^{(3)}9\omega_1^2\left\{\Omega_p^{(1)+}e^{ik_p^{(1)}(z-z_{p-1})} + \Omega_p^{(1)-}e^{-ik_p^{(1)}(z-z_{p-1})}\right\}^3\\
&= -\mu\varepsilon_0\chi^{(3)}9\omega_1^2\left\{\left[\Omega_p^{(1)+}\right]^3e^{i3k_p^{(1)}(z-z_{p-1})} + \left[\Omega_p^{(1)-}\right]^3e^{-i3k_p^{(1)}(z-z_{p-1})}\right.\\
&\quad \left. + 3\left[\Omega_p^{(1)+}\right]^2\left[\Omega_p^{(1)-}\right]e^{ik_p^{(1)}(z-z_{p-1})} + 3\left[\Omega_p^{(1)+}\right]\left[\Omega_p^{(1)-}\right]^2e^{-ik_p^{(1)}(z-z_{p-1})}\right\},
\end{aligned} \tag{7}$$

where $k_p^{(3)} = n_p^{(3)}k_0^{(3)}$, $k_0^{(3)} = 3\omega_1/\mathrm{c}$, and $n_p^{(3)}$ represents the refractive index corresponding to the THW field within the pth layer. The right-hand side of Eq. (7) represents the THW source induced by the nonlinear coefficient $\chi^{(3)}$. By solving Eq. (7), the electric field distribution in the pth layer can be obtained in Eq. (8)

$$\begin{aligned}
E_p^{(3)}(z) &= E_p^{(3)+}e^{ik_p^{(3)}(z-z_{p-1})} + E_p^{(3)-}e^{-ik_p^{(3)}(z-z_{p-1})} + G_p\left(\Omega_p^{(1)+}\right)^3e^{i3k_p^{(1)}(z-z_{p-1})} + G_p\left(\Omega_p^{(1)-}\right)^3e^{-i3k_p^{(1)}(z-z_{p-1})}\\
&\quad + 3R_p\left(\Omega_p^{(1)+}\right)^2\left(\Omega_p^{(1)-}\right)e^{ik_p^{(1)}(z-z_{p-1})} + 3R_p\left(\Omega_p^{(1)+}\right)\left(\Omega_p^{(1)-}\right)^2e^{-ik_p^{(1)}(z-z_{p-1})}.
\end{aligned} \tag{8}$$

The $E_p^{(3)\pm}$ represents the amplitudes of the forward- and backward-propagating THW. The coefficients G_p and R_p are given by the following expressions:

$$G_p = \frac{-9\omega_1^2\mu\varepsilon_0\chi^{(3)}}{k_p^{(3)2} - 9k_p^{(1)2}}, \quad R_p = \frac{-9\omega_1^2\mu\varepsilon_0\chi^{(3)}}{k_p^{(3)2} - k_p^{(1)2}}.$$

From the equation $\nabla \times E = ik_0 H$, we can obtain the magnetic field $H_p^{(3)}(z)$,

$$\begin{pmatrix} E_p^{(3)}(z) \\ H_p^{(3)}(z) \end{pmatrix} = \begin{pmatrix} 1 & 1 \\ n_p^{(3)} & -n_p^{(3)} \end{pmatrix} \begin{pmatrix} E_p^{(3)+}(z) \\ E_p^{(3)-}(z) \end{pmatrix} + \begin{pmatrix} 1 & 1 \\ \frac{3n_p^{(1)}k_0^{(1)}}{k_0^{(3)}} & -\frac{3n_p^{(1)}k_0^{(1)}}{k_0^{(3)}} \end{pmatrix} \begin{pmatrix} G_p\left[\Omega_p^{(1)+}(z)\right]^3 \\ G_p\left[\Omega_p^{(1)-}(z)\right]^3 \end{pmatrix}$$
$$+ \begin{pmatrix} 1 & 1 \\ \frac{n_p^{(1)}k_0^{(1)}}{k_0^{(3)}} & -\frac{n_p^{(1)}k_0^{(1)}}{k_0^{(3)}} \end{pmatrix} \begin{pmatrix} 3R_p\left[\Omega_p^{(1)+}(z)\right]^2\left[\Omega_p^{(1)-}(z)\right] \\ 3R_p\left[\Omega_p^{(1)+}(z)\right]\left[\Omega_p^{(1)-}(z)\right]^2 \end{pmatrix}. \tag{9}$$

Equations (9) and (3) have significant differences. The first term on the right side of Eq. (9) is commonly referred to as the "free wave" as it represents the amplitude of the THW. The second and third terms indicate the amplitude of the "bound wave" of THW. The first arises from the forward and backward FW fields, while the second captures the effects resulting from the mutual interference between the forward- and backward-FW fields on THW. To achieve a more concise representation of the obtained results, the aforementioned matrices in Eq. (9) are defined as follows:

$$\boldsymbol{A}_p = \begin{pmatrix} 1 & 1 \\ n_p^{(3)} & -n_p^{(3)} \end{pmatrix}, \quad \boldsymbol{C}_p = \begin{pmatrix} 1 & 1 \\ \frac{3n_p^{(1)}k_0^{(1)}}{k_0^{(3)}} & -\frac{3n_p^{(1)}k_0^{(1)}}{k_0^{(3)}} \end{pmatrix},$$
$$\boldsymbol{F}_p = \begin{pmatrix} 1 & 1 \\ \frac{n_p^{(1)}k_0^{(1)}}{k_0^{(3)}} & -\frac{n_p^{(1)}k_0^{(1)}}{k_0^{(3)}} \end{pmatrix}.$$

Building upon the aforementioned methodology, the periodic unit $(n_1 n_2)$ is situated within a medium of air, enabling us to determine the plane wave coefficients $E^{(3)\pm}$ governing the THW through careful consideration of the boundary conditions. On the left side of the unit $(n_1 n_2)$, the following relationship is established:

$$\boldsymbol{A}_0 \begin{pmatrix} E_{2j-2^-}^{(3)+} \\ E_{2j-2^-}^{(3)-} \end{pmatrix} = \boldsymbol{A}_1 \begin{pmatrix} E_{2j-2^+}^{(3)+} \\ E_{2j-2^+}^{(3)-} \end{pmatrix} + \boldsymbol{C}_1 \begin{pmatrix} G_p(\boldsymbol{\Omega}_{2j-2^+}^{+})^3 \\ G_p(\boldsymbol{\Omega}_{2j-2^+}^{-})^3 \end{pmatrix} + \boldsymbol{F}_1 \begin{pmatrix} 3R_p(\boldsymbol{\Omega}_{2j-2^+}^{+})^2(\boldsymbol{\Omega}_{2j-2^+}^{-}) \\ 3R_p(\boldsymbol{\Omega}_{2j-2^+}^{+})(\boldsymbol{\Omega}_{2j-2^+}^{-})^2 \end{pmatrix}. \tag{10}$$

On the right side of the unit $(n_1 n_2)$, the following relationship is established:

$$\boldsymbol{A}_0 \begin{pmatrix} E_{2j-2^-}^{(3)+} \\ E_{2j-2^-}^{(3)-} \end{pmatrix} = \boldsymbol{A}_2\boldsymbol{L}_2\boldsymbol{A}_2^{-1}\boldsymbol{A}_1\boldsymbol{L}_1 \begin{pmatrix} E_{2j-2^+}^{(3)+} \\ E_{2j-2^+}^{(3)-} \end{pmatrix} + \boldsymbol{A}_2\boldsymbol{L}_2\boldsymbol{A}_2^{-1}\boldsymbol{C}_1\boldsymbol{K}_1 \begin{pmatrix} G_p(\boldsymbol{\Omega}_{2j-2^+}^{+})^3 \\ G_p(\boldsymbol{\Omega}_{2j-2^+}^{-})^3 \end{pmatrix}$$
$$+ \boldsymbol{A}_2\boldsymbol{L}_2\boldsymbol{A}_2^{-1}\boldsymbol{F}_1\boldsymbol{U}_1 \begin{pmatrix} 3R_p(\boldsymbol{\Omega}_{2j-2^+}^{+})^2(\boldsymbol{\Omega}_{2j-2^+}^{-}) \\ 3R_p(\boldsymbol{\Omega}_{2j-2^+}^{+})(\boldsymbol{\Omega}_{2j-2^+}^{-})^2 \end{pmatrix}. \tag{11}$$

The related matrices in Eq. (11) are defined as

$$\boldsymbol{L}_p = \begin{pmatrix} e^{ik_p^{(3)}d_p} & 0 \\ 0 & e^{-ik_p^{(3)}d_p} \end{pmatrix} \boldsymbol{U}_p = \begin{pmatrix} e^{ik_p^{(1)}d_p} & 0 \\ 0 & e^{-ik_p^{(1)}d_p} \end{pmatrix}$$
$$\boldsymbol{K}_p = \begin{pmatrix} e^{i3k_p^{(1)}d_p} & 0 \\ 0 & e^{-i3k_p^{(1)}d_p} \end{pmatrix}.$$

By combining Eqs. (10) and (11), the THW distribution on both sides of the periodic unit $(n_1 n_2)$ can be obtained. By utilizing Eq. (12), the THW field emitted from both sides can be computed when the periodic unit $(n_1 n_2)$ is placed in the air

$$\begin{pmatrix} E_{2j^+}^{(3)+} \\ 0 \end{pmatrix} = A_0^{-1}\boldsymbol{A}_2\boldsymbol{L}_2\boldsymbol{A}_2^{-1}\boldsymbol{A}_1\boldsymbol{L}_1\boldsymbol{A}_1^{-1}\boldsymbol{A}_0 \begin{pmatrix} 0 \\ E_{2j-2^+}^{(3)-} \end{pmatrix}$$
$$+ \boldsymbol{A}_0^{-1}\left(\boldsymbol{A}_2\boldsymbol{L}_2\boldsymbol{A}_2^{-1}\boldsymbol{C}_1\boldsymbol{K}_1 - \boldsymbol{A}_2\boldsymbol{L}_2\boldsymbol{A}_2^{-1}\boldsymbol{A}_1\boldsymbol{L}_1\boldsymbol{A}_1^{-1}\boldsymbol{C}_1\right) \begin{pmatrix} G_p(\boldsymbol{\Omega}_{2j-2^+}^{+})^3 \\ G_p(\boldsymbol{\Omega}_{2j-2^+}^{-})^3 \end{pmatrix}$$
$$+ \boldsymbol{A}_0^{-1}\left(\boldsymbol{A}_2\boldsymbol{L}_2\boldsymbol{A}_2^{-1}\boldsymbol{F}_1\boldsymbol{U}_1 - \boldsymbol{A}_2\boldsymbol{L}_2\boldsymbol{A}_2^{-1}\boldsymbol{A}_1\boldsymbol{L}_1\boldsymbol{A}_1^{-1}\boldsymbol{F}_1\right) \begin{pmatrix} 3R_p(\boldsymbol{\Omega}_{2j-2^+}^{+})^2(\boldsymbol{\Omega}_{2j-2^+}^{-}) \\ 3R_p(\boldsymbol{\Omega}_{2j-2^+}^{+})(\boldsymbol{\Omega}_{2j-2^+}^{-})^2 \end{pmatrix}. \tag{12}$$

B. TMM FOR PERIODIC CASE

Having gained a comprehensive understanding of employing TMM for examining the FW field distribution within periodic unit (n_1n_2) and elucidating the THW, the subsequent endeavor involves the derivation of the TMM to investigate the characteristics of THW propagation across the entirety of the HS through an iterative scheme.

The spatial distribution of the FW field throughout every individual layer encompassing the HS can be effectively derived by employing Eq. (5). The $E_t^{(1)-} = 0$ implies the nonexistence of backwards wave propagation at the right side of the HS

$$\begin{pmatrix} E_t^{(1)+} \\ 0 \end{pmatrix} = \boldsymbol{Q}_0^{-1}\left(\boldsymbol{Q}_2\boldsymbol{M}_2\boldsymbol{Q}_2^{-1}\boldsymbol{Q}_1\boldsymbol{M}_1\boldsymbol{Q}_1^{-1}\right)^N \boldsymbol{Q}_0 \begin{pmatrix} E_0^{(1)+} \\ E_0^{(1)-} \end{pmatrix}. \quad (13)$$

Equation (12) serves as the unit transfer matrix for the jth periodic unit (n_1n_2) within the entirety of the HS. Considering the overall periodic nature of the HS, the utilization of this equation facilitates the derivation of the comprehensive transfer matrix pertaining to the THW field

$$\begin{aligned} \begin{pmatrix} E_t^{(3)+} \\ 0 \end{pmatrix} = A_0^{-1}\boldsymbol{S}^N\boldsymbol{A}_0\begin{pmatrix} 0 \\ E_0^{(3)-} \end{pmatrix} + \sum_{j=1}^{N}\boldsymbol{A}_0^{-1}\boldsymbol{S}^{N-j}\Bigg\{\left(\boldsymbol{A}_2\boldsymbol{L}_2\boldsymbol{A}_2^{-1}\boldsymbol{C}_1\boldsymbol{K}_1 - \boldsymbol{S}\boldsymbol{C}_1\right)\begin{pmatrix} G_p(\boldsymbol{\Omega}_{2j-2^+}^{+})^3 \\ G_p(\boldsymbol{\Omega}_{2j-2^+}^{-})^3 \end{pmatrix} \\ + \left(\boldsymbol{A}_2\boldsymbol{L}_2\boldsymbol{A}_2^{-1}\boldsymbol{F}_1\boldsymbol{U}_1 - \boldsymbol{S}\boldsymbol{F}_1\right)\begin{pmatrix} 3R_p(\boldsymbol{\Omega}_{2j-2^+}^{+})^2(\boldsymbol{\Omega}_{2j-2^+}^{-}) \\ 3R_p(\boldsymbol{\Omega}_{2j-2^+}^{+})(\boldsymbol{\Omega}_{2j-2^+}^{-})^2 \end{pmatrix}\Bigg\}, \end{aligned} \quad (14)$$

where $\boldsymbol{S} = \boldsymbol{A}_2\boldsymbol{L}_2\boldsymbol{A}_2^{-1}\boldsymbol{A}_1\boldsymbol{L}_1\boldsymbol{A}_1^{-1}$. By virtue of Eq. (14), the emanation of the THW field propagating from opposing facets of the HS can be ascertained. Consequently, a methodology has been successfully formulated that embraces the employment of the TMM to scrutinize THW generation within the HS. The THW conversion efficiency is defined as

$$\eta_{\text{con.effi.}} = \left|\frac{E_t^{(3)+}}{E_0}\right|^2 + \left|\frac{E_0^{(3)-}}{E_0}\right|^2. \quad (15)$$

III. RESULTS AND DISCUSSION

The constructed HS is assembled by stacking unit cells composed of CS_2 and K9 glass. Accounting for the influence of dispersion, experimental testing reveals that the refractive index of K9 glass corresponds to $n_2^{(1)} = 1.512$ at the FW wavelength and $n_2^{(3)} = 1.63$ at the THW wavelength. Similarly, $n_1^{(1)} = 3.6$ and $n_1^{(3)} = 3.87$, as well as a nonlinear coefficient of $\chi^{(3)} = 5.442 \times 10^{-20}\ m^2/V^2$, are observed [39]. To realize the conversion between the FW field and the THW field, conventional techniques merely necessitate satisfying the QPM condition [17,18]. However, with the introduction of periodic refractive index modulation, plane waves propagating towards the interface undergo a shift and are influenced by PBGs. Furthermore, within the HS, the THW field generated by nonlinear polarization undergoes multiple reflections [26]. Consequently, deriving an explicit expression for QPM becomes more intricate. Henceforth, a numerical approach is employed which involves the manipulation of the medium thickness to directly achieve QPM.

In Fig. 2, the conversion efficiency achieves a maximal magnitude of 1.76% at $d = 3217.7$ nm. As the d undergoes a decrement, there emerges an escalating pattern in the conversion efficiency, accompanied by a commensurate amplification in the extent of change. During this conventional process, a successive enhancement of 0.21%, 0.31%, 0.42%, and 0.41% is observed. The diminishing degree of adjustment for d reflects that only more precise structural QPM can achieve greater perfection. Moreover, with diminishing full width at half maximum, the prerequisites for QPM manifest heightened stringency, as evidenced by the apex positioned at the extreme lift of the graphical representation. Although this pinnacle solely yields a conversion efficiency of a mere 0.41%, it affords a broader array of adaptable thickness parameters that adhere to the requisites for QPM within the permissible scope. Additionally, differentials in conversion efficiency across distinct matching points arise from the proximity of the incident wavelength to the edge of the PBGs, coupled with the acuity of the diverse resonant modes proximate to the PBGs peripheries. The disparity in intensity observed among resonant modes situated at the periphery of a PBG can be accounted for by the following reasons: certain specific resonant modes may exhibit a greater degree of spatial confinement of the optical field, consequently giving rise

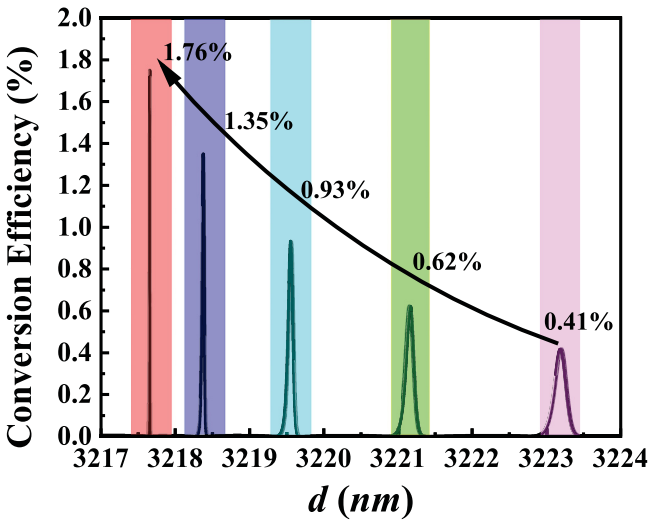

FIG. 2. The variation of conversion efficiency with parameter d (where $d = d_1 + d_2$, and $d_1 = 900$ nm). In this scenario, the incident wave is characterized by a wavelength $\lambda_{\text{wave}} = 889.9$ nm, and the pump light electric field E_0 and N are set to 2.0×10^9 V/m [39] and 50, respectively.

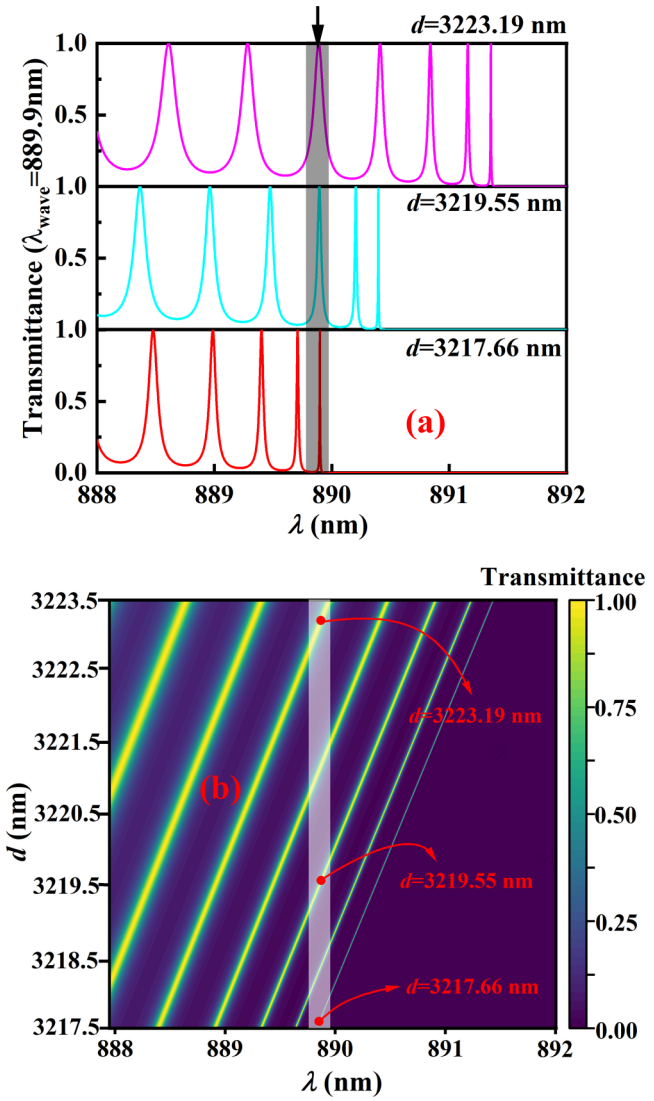

FIG. 3. (a) The transmittance corresponding to specific values of three parameter sets (d) within the wavelength range of 888 nm to 892 nm. (b) When the λ_{wave} fixed at 889.9 nm, the various resonant modes overlap with the λ_{wave} as the parameters of d vary.

to heightened energy density and amplified intensity, by extension. Moreover, there exist coupling phenomena between these resonant modes. As a consequence of this coupling, the intensity of particular modes can experience an increase, while the intensity of other modes may conversely diminish.

With the λ_{wave} held constant, adjustment of the parameter d allows for manipulation of the PBGs positions. This permits precise alignment of the incident wavelength λ_{wave} with neighboring and distinct resonant peaks, albeit limited to the display of only the adjacent five resonant peaks near the PBGs edges due to space constraints. The $\lambda_{wave} = 889.9$ nm, indicated by the shaded grey region within Figs. 3(a) and 3(b). Notably, during the transitional phase from 3217.66 nm to 3223.19 nm, when d attains a value of 3217.66 nm, the λ_{wave} harmonizes precisely with the resonant peak positioned nearest to the edges of PBGs. In Fig. 3(b), the resonant mode corresponding to the conversion efficiency shown in Fig. 2 is displayed and each resonant peak exhibits a transmittance

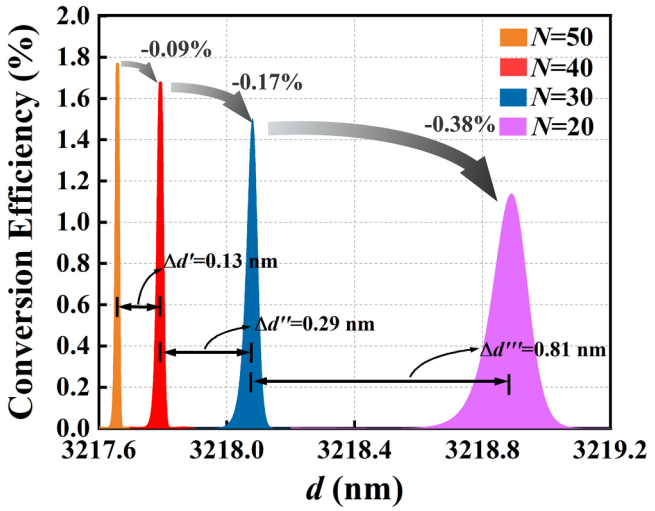

FIG. 4. The impact of the period number N, denoted as 50, 40, 30, or 20, on both the conversion efficiency and the location of the matching point is examined. The four different colored curves represent the observed conversion peaks under optimal matching conditions. The displayed conversion peaks are generated by the resonant mode closest to the PBG edge, omitting the conversion peaks produced by other resonant modes.

exceeding 0.98. The variance in conversion efficiency at each point stems from the position and intensity of the resonant peaks. Resonant modes situated proximate to the PBGs edge showcase enhanced strength, accompanied by an augmentation in group delay. Consequently, THW experiences lengthier response times and yields higher conversion efficiency in the vicinity of the edge relative to other positions. Moreover, the HS characterized by a greater number of stacked periods manifest more pronounced PBGs and sharper resonances.

Upon analysis of Fig. 4, a discernible trend emerges the conversion efficiency at the optimal matching point experiences successive declines of 0.09%, 0.17%, and 0.38% as the period number N decreases from 50 to 40, to 30 and eventually to 20. Additionally, the intervals between different matching points grow larger as the parameter-d varies. In the transition from $N = 50$ to $N = 40$, the interval amounts to 0.13 nm. Similarly, when transitioning from $N = 30$ to $N = 20$, the interval expands to 0.81 nm. These findings align harmoniously with the previously discussed arguments, substantiating that the reduction in the N diminishes the intensity of electric field resonance modes at the PBGs edges. Consequently, this decrement adversely affects the overall conversion efficiency.

It is widely acknowledged that the efficacy of THW conversion efficiency is not solely contingent upon QPM conditions but is also linked to the electric field strength of the incident pump light. Figure 5 presents a visual representation delineating the functional correlation between pump light strength and THW conversion efficiency. As the electric field strength of the pump light varies within the range of 1.7×10^9 V/m to 2.1×10^9 V/m, the conversion efficiency ascends from 0.92% to 2.15%. By fitting the given results, a rough linear relationship describing this variation can be approximated. The conversion efficiency is directly proportional to the strength of the incident pump wave. In the realm of nonlinear optics,

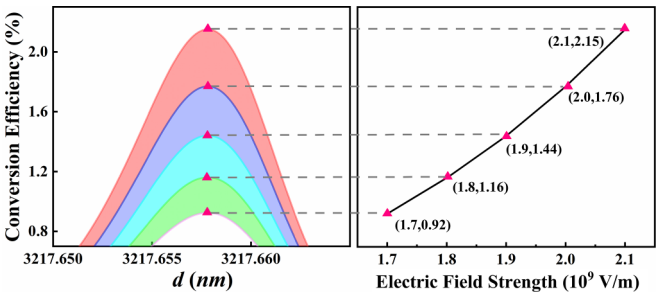

FIG. 5. The left panel showcases the augmentation in conversion efficiency with the escalation of electric field strength at the QPM point, specifically targeting the resonance peak closest to the PBGs edge with the parameter $d = 3217.66$ nm. On the other hand, the right panel exhibits the linear fitting curves for both variables, providing an effective visualization of their relationship.

when the pump light interacts with the medium, it initiates photon interactions and facilitates energy transfer. These interactions are typically accomplished through the utilization of nonlinear polarization effects, wherein the response of the medium becomes more pronounced as the electric field intensity increases [26]. Accordingly, within the process of THW generation, higher intensities of the pump light actively contribute to the conversion of a greater number of photons into harmonic photons through nonlinear processes. Consequently, an increase in the strength of the pump light results in an enhancement of the conversion efficiency.

In addition, the internal distribution of the fundamental wave electric field intensity within the nonlinear medium significantly affects the intensity of the P^{NL}. Figure 6(a) illustrates the intensity of the FW at different positions within the HS. Due to refractive index mismatch within the layered structure, multiple reflections of the EM waves are inevitable, leading to pronounced interference between the reflected waves at different interfaces. It is evident that the FW electric field undergoes several-fold amplification throughout the propagation process. The distribution of the THW electric field within the HS is shown in Fig. 6(b). Due to the periodic distribution of the nonlinear medium, the variation of the THW within the HS is more uniform compared to the FW. It is worth noting that the electric field of the THW not only depends on the intensity of the FW, as mentioned earlier, but also incorporates contributions from the "free wave" amplitude and "bound wave" amplitude.

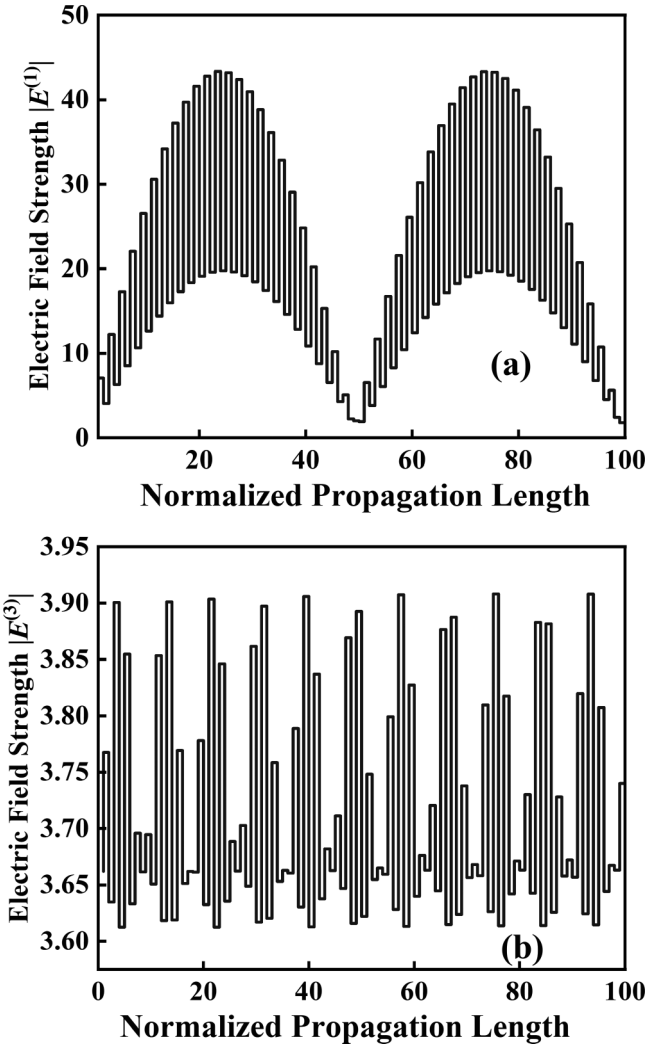

FIG. 6. When $\lambda_{wave} = 889.9$ nm, (a) the spatial distribution of the FW electric field intensity inside the HS varies with the normalized propagation length (normalized by the incident electric field intensity). (b) The spatial distribution of the THW electric field intensity inside the HS varies with the normalized propagation length (normalized by the backward-transmitted THW intensity, and the propagation length is normalized by the thickness of each medium layer).

IV. CONCLUSION

In this paper, a method grounded in the transfer matrix was devised, enabling an exploration of the THG within a layered HS composed of materials exhibiting nonlinearity. By considering multiple reflections and interference, a procedure was provided that allows for the computation of both forward- and backward-propagation of the THW. In situations where the lengths of the samples are akin, a comparative analysis with the customary QPM scheme has evinced the amplification of the nonlinear processes engendered by this novel HS. Such enhancement can be ascribed to the harnessing of potent electric field energies and locally augmented electromagnetic mode densities, which are proximate to the PBGs. Furthermore, a direct pathway to optimizing parameters is offered, thereby enhancing the conversion efficiency, considering the intricate nature of the field dynamics characteristic of the HS. The distinct optical characteristics and energy conversion capabilities of THW have played a crucial role in advancing optical imaging, spectroscopy, biomedical applications, and laser technology. In light of these contributions, our research endeavors will be centered around the enhancement of harmonic conversion efficiency.

ACKNOWLEDGMENTS

This work was supported by the Postgraduate Research and Practice Innovation Program of Jiangsu Province (Grant No. KYCX24_1160).

[1] K. M. Ho, C. T. Chan, and C. M. Soukoulis, Phys. Rev. Lett. **65**, 3152 (1990).
[2] D. Cassagne, C. Jouanin, and D. Bertho, Phys. Rev. B **53**, 7134 (1996).
[3] L. Y. Cui, X. Li, J. Chen, Y. Y. Cao, G. Q. Du, and J. Ng, Phys. Rev. A **96**, 023833 (2017).
[4] O. Peyrusse, P. Jonnard, and J.-M. André, Phys. Rev. A **103**, 043508 (2021).
[5] G. Lehmann and K. H. Spatschek, Phys. Rev. Lett. **116**, 225002 (2016).
[6] J. Peřina, M. Centini, C. Sibilia, M. Bertolotti, and M. Scalora, Phys. Rev. A **73**, 033823 (2006).
[7] M. Corona and A. B. U'Ren, Phys. Rev. A **76**, 043829 (2007).
[8] S. R. Entezar, A. Namdar, Z. Eyni, and H. Tajalli, Phys. Rev. A **78**, 023816 (2008).
[9] L. Y. Cui, G. Q. Du, and J. Ng, Phys. Rev. A **102**, 023502 (2020).
[10] Z. Y. Li and L. L. Lin, Phys. Rev. E **67**, 046607 (2003).
[11] L. M. Qi, Z. Q. Yang, F. Lan, X. Gao, and Z. J. Shi, Phys. Plasmas **17**, 042501 (2010).
[12] Z. Y. Li, J. Wang, and B. Y. Gu, Phys. Rev. B **58**, 3721 (1998).
[13] S. Sadhukhan and S. Ghosh, Phys. Rev. A **108**, 023511 (2023).
[14] A. C. Araújo, S. Azevedo, C. Furtado, A. J. Chaves, C. H. Costa, and C. G. Bezerra, Phys. Rev. A **104**, 053532 (2021).
[15] F. Loran and A. Mostafazadeh, Phys. Rev. A **93**, 042707 (2016).
[16] F. Loran and A. Mostafazadeh, Phys. Rev. A **104**, 032222 (2021).
[17] D. S. Bethune, J. Opt. Soc. Am. B **6**, 910 (1989).
[18] D. S. Bethune, J. Opt. Soc. Am. B **8**, 367 (1991).
[19] N. Hashizume, O. Makoto, K. Takashi, and I. Ryoichi, J. Opt. Soc. Am. B **12**, 1894 (1995).
[20] G. I. Stegeman and C. T. Seaton, J. Appl. Phys. **58**, R57 (1985).
[21] P. Yeh, J. Opt. Soc. Am. **69**, 742 (1979).
[22] S. D. Gupta and G. S. Agarwal, Opt. Commun. **103**, 122 (1993).
[23] D. Sarid, Phys. Rev. Lett. **47**, 1927 (1981).
[24] G. S. Agarwal and S. D. Gupta, Phys. Rev. B **34**, 5239 (1986).
[25] S. D. Gupta and G. S. Agarwal, J. Opt. Soc. Am. B **4**, 691 (1987).
[26] J. J. Li, Z. Y. Li, and D. Z. Zhang, Phys. Rev. E **75**, 056606 (2007).
[27] M. L. Ren and Z. Y. Li, J. Opt. Soc. Am. B **27**, 1551 (2010).
[28] U. R. Meza, B. S. Mendoza, and W. L. Mochán, Phys. Rev. B **99**, 125408 (2019).
[29] G. Shoulga, G. R. Barir, and A. Bahabad, Phys. Rev. A **106**, L031502 (2022).
[30] T. T. Wu, Y. Luo, S. A. Maier, and L. Wei, Phys. Rev. Appl. **11**, 014049 (2019).
[31] D. Smirnova, S. Kruk, D. Leykam, E. Melik-Gaykazyan, D. Y. Choi, and Y. Kivshar, Phys. Rev. Lett. **123**, 103901 (2019).
[32] F. Giorgianni, E. Chiadroni, A. Rovere, M. Cestelli-Guidi, A. Perucchi, M. Bellaveglia, M. Castellano, D. Di Giovenale, G. Di Pirro, M. Ferrario, R. Pompili, C. Vaccarezza, F. Villa, A. Cianchi, A. Mostacci, M. Petrarca, M. Brahlek, N. Koirala, S. Oh, and S. Lupi, Nat. Commun. **7**, 11421 (2016).
[33] N. Yoshikawa, T. Tomohiro, and T. Koichiro, Science **356**, 736 (2017).
[34] R. E. F. Silva, Á. Jiménez-Galán, B. Amorim, O. Smirnova, and M. Ivanov, Nat. Photon. **13**, 849 (2019).
[35] A. Chacón, D. Kim, W. Zhu, S. P. Kelly, A. Dauphin, E. Pisanty, A. S. Maxwell, A. Picón, M. F. Ciappina, D. E. Kim, C. Ticknor, A. Saxena, and M. Lewenstein, Phys. Rev. B **102**, 134115 (2020).
[36] S. Ghimire, A. D. DiChiara, E. Sistrunk, P. Agostini, L. F. DiMauro, and D. A. Reis, Nat. Phys. **7**, 138 (2011).
[37] T. Otobe, Phys. Rev. B **94**, 235152 (2016).
[38] Y. S. You, D. A. Reis, and S. Ghimire, Nat. Phys. **13**, 345 (2017).
[39] Z. X. Tang, W. Yi, J. Pan, Y. H. Zou, S. C. Wen, A. Danner, and C. W. Qiu, Opt. Express **23**, 19885 (2015).
[40] V. Mahalakshmi, J. Jose, and S. D. Gupta, Pramana **47**, 317 (1996).